Supplementary Information

Compressing Liquid Nanofoam System: Liquid Infiltration or Nanopore Deformation?

Yue Zhang[1#], Mingzhe Li[2#], Yuan Gao[1], Baoxing Xu [1*], Weiyi Lu[2*]

[1] Department of Mechanical and Aerospace Engineering, University of Virginia, Charlottesville, VA 22904, USA

[2] Department of Civil and Environmental Engineering, Michigan State University, East Lansing, MI 48824, USA

S1. Details of simulation method

In this study, we used molecular dynamics (MD) simulation to explore useful insights into the complex behaviors of liquid infiltration into flexible nanopore. The simulations were performed using the LAMMPS (large-scale atomic/molecular massively parallel simulator) package. Water was considered as the liquid phase and silica nanotube (SNT) was adopted as a model structure of the cylindrical nanopore. The water model was an extended simple point charge (SPC/E) model. Tersoff potential was utilized to model the flexible SNT, which took the form

$$E = \lambda E_0 = \lambda\{\frac{1}{2}\sum_i\sum_{j\neq i} f_c(r_{ij})[f_R(r_{ij}) + b_{ij}f_A(r_{ij})]\} \quad (1)$$

Where f_R is a repulsive two-body term while f_A is an attractive three-body term managed by the b_{ij} bond function. And λ is a tuning factor used to tune the total deformation energy of SNT, in order to realize the adjustment of buckling pressures of SNT. The 12-6 Lennard-Jones (L-J) empirical force field and a Coulomb potential were used to describe the intermolecular potential between atoms

$$E(r_{ij}) = 4\varepsilon[(\sigma/r_{ij})^{12} - (\sigma/r_{ij})^{6}] + q_i q_j/r_{ij} \quad (2)$$

where r_{ij} denotes the distance between atom i and j, σ and ε are the equilibrium distance and

# These two authors contribute equally
*Corresponding authors: wylu@egr.msu.edu (WL), and bx4c@virginia.edu (BX)

the interactive well depth of the potential, q_i and q_j are the partial charge assigned to atom i and j, respectively. In this study, the value of well depth ε_{si-o} was tuned to realize different wettability condition of the SNT, which is shown in **Figure S1**. The cut-off radius was chosen 1.0 nm for all L-J interactions to calculate the short-range van der Waals forces, and the particle-particle-particle-mesh (PPPM) algorithm with a root mean of 0.0001 was used to handle the long range Coulomb interactions. Unless otherwise stated, all simulations were performed in NVT ensemble with Nose/Hoover thermostat at temperature 300 K.

S2. Determination of critical infiltration pressure

In the MD simulations, a rigid SNT with diameter of D was immersed in a reservoir filled with the water molecules. The initial density of water inside the reservoir was chosen to that of bulk water, $\rho_0 = 998.0\ kg/m^3$ by adjusting the total number of water molecules. The left and right surfaces of the reservoir were bounded by two rigid walls, with the right one fixed and the left one movable to mimic a piston. A periodic boundary condition was imposed on the other four lateral planes of the computational cell. After initial calculation to minimize system energy, we first carried out equilibrium simulations through relaxation and thermalization of the system to 300 K with a time step of 1.0 fs for 0.5 ns. During this equilibration state, the water molecules stayed outside the SNT due to its hydrophobic nature. After that, the piston starts to move, the water phase was pressurized and the pressure in the reservoir built up simultaneously.

When the pressure is relatively low, only very few water molecules are oscillated near the entrance of the SNT. When the water pressure P exceeds a critical value, P_{in}, the highly compressed water molecules will begin to infiltrate and wet inside the SNT. Afterward, the pressure comes to a plateau stage. The variation of the number of infiltrated water molecules as a function of applied pressure for a SNT with tube diameter $D = 1.4nm$ is shown in **Figure S2 (a)**. And the Laplace-Young equation can be applied at the nanoscale to correlate the infiltration pressure P_{in} with surface tension γ, which is $P_{in} = \frac{-4\gamma[cos\theta]}{D}$, where θ is the

contact angle between wall surface of nanotube and water molecules and represents the surface wettability of nanotube. Therefore, the surface tension $\gamma = 100.75MPa \cdot nm$ can be obtained from the MD simulation results as shown in **Figure S2 (b)**.

S3. Determination of critical buckling pressure for solid nanotube

In the MD simulations, a flexible SNT with length of L and diameter of D was first energy-minimized and thermally equilibrated before the simulation of compression was run. After the SNT reached the equilibrium state, an axially quasi-static compressive displacement loading was imposed on both end of the SNT. As shown in **Figure S3 (a)**, at the initial elastic stage, the compressive stress σ increases almost linearly with the strain $|\varepsilon|$, and when the stress comes to a critical value, the stress will drop suddenly, which indicates the axial buckling of SNT occurs. And the classic buckling theory can be applied to determine this critical axial buckling pressure ${P_{axial}}^{cr} = \frac{C_1\lambda(D2 + h2)}{L2}$, where h is the thickness of nanotube wall and $C_1\lambda$ is an elastic constant of relevance to the axial compressive stiffness of nanotube. Consider a pristine silica nanotube (SNT) with diameter of $D = 1.4nm$ and $\lambda = 1$, $C_1 = 159.16GPa$ can be obtained from the MD simulation results as shown in **Figure S3 (b)**.

Similarly, to determine the critical radial buckling pressure, a flexible SNT with both end capped was immersed in the water phase. After the initial equilibrium state, the water reservoir was compressed by a piston, and a hydrostatic pressure in the water environment will be generated to mimic a uniform pressure applied on the SNT. As shown in **Figure S4 (a)**, at the initial elastic stage, the applied pressure increases almost linearly with the simulation time, and when the pressure comes to a critical value, it will drop suddenly, which indicates the radial buckling of SNT occurs. And the classic buckling theory can be applied to determine this critical radial buckling pressure ${P_{radial}}^{cr} = \frac{C_2\lambda}{D3}$, where $C_2\lambda$ is an elastic constant of relevance to the radial stiffness of nanotube. Consider a pristine silica nanotube (SNT) with $\lambda = 1$, $C_2 = 1.93GPa \cdot nm^3$ can be obtained from the MD simulation as shown in **Figure S4 (b)**. The variation of critical buckling pressure with deformation energy tuning factor λ is also shown in **Figure S5**.

S4. Details of experimental method

The nanoporous material used in this study was a silica gel with silicone treated hydrophobic surface (Perform-O-Sil 668, Nottingham Corp.). The material was in powder form, with an average particle size of 4 μm. The average pore diameter was 115 nm, characterized by the water porosimetry technique and SEM.

In a stainless-steel cylinder, 0.2 g of the nanoporous silica gel was first pre-compressed to various peak forces without the presence of liquid at a constant rate of 1 mm/min by a universal tester (Model 5982, Instron, Inc.). Once the peak force was reached, the crosshead of the Instron machine was moved back at the same velocity. The peak forces applied on different silica gel samples were 0.25 kN, 0.50 kN and 0.75 kN, respectively. The cross-sectional area of the pistons, A, was 126 mm^2. Thus, the applied peak stress, σ_{max}, were 2 MPa, 4 MPa, and 6 MPa accordingly.

Pressure-induced liquid infiltration tests were conducted on all the silica gel particles, with or without pre-compression, based liquid nanofoam (LN) systems. In the stainless-steel cylinder, 2 g of saturated lithium chloride (LiCl) aqueous solution (46 wt%) was slowly dropped on the silica gel samples to minimize air bubbles trapped in the LN specimens. Since the silica gel particles were hydrophobic, they were not soaked up by the aqueous solution at ambient condition. The LN sample was sealed by two pistons with O-rings. The upper piston was driven into the cylinder by the Instron machine at a constant rate of 1 mm/min. When the internal pressure reached 9 MPa, the piston was moved back at the same speed. The friction between O-ring and cylinder wall was minimized by high vacuum grease and no leaking was observed during all infiltration tests. The applied pressure was calculated as $P=F/A$, where F was the force applied on the piston. The specific volume change of the LN sample was defined as $\Delta V=A\cdot\delta/m$, where δ and m were the displacement of the piston and the mass of the silica gel, respectively. Part of the ions in the saturated LiCl aqueous solution was trapped in the nanopores during the first loading-unloading cycle, which would affect the second loading-unloading cycles. To remove these residual electrolytes in nanopores, the silica gel samples were separated from the saturated LiCl solution by filtering, thoroughly rinsed by large amount

of ethanol and warm DI water, and then dried in air at 80 ˚C for 48 h. The second pressure-induced liquid infiltration tests were conducted on the recycled nanoporous silica gel based LN systems. The mass ration between the nanoporous silica gel and the saturated LiCl aqueous solution was the same.

S5. Water Porosimetry and SEM characterization on pore size distribution

The pore size distribution of the nanoporous silica gel was characterized by water porosimetry and SEM. In a typical water porosimetry characterization, DI water was used as the non-wettable liquid intruded into the hydrophobic nanopores. As shown in **Figure S9 (a)**, the cumulative pore volume distribution of the intruded water was measured as a function of the applied pressure, from which the pore size distribution of the silica gel can be calculated by using the Laplace-Young equation. The resulted pore size distribution is shown in **Figure S9 (b)**.

The results were further verified by the SEM photos of nanoporous particles as shown in **Figure S10**. From the figure, the nanopores, surrounded by the solid frame, possessed irregular shapes. Besides, the pores were highly interconnected with each other from the surface to the center of the particles, forming 3-D nanoporous structures.

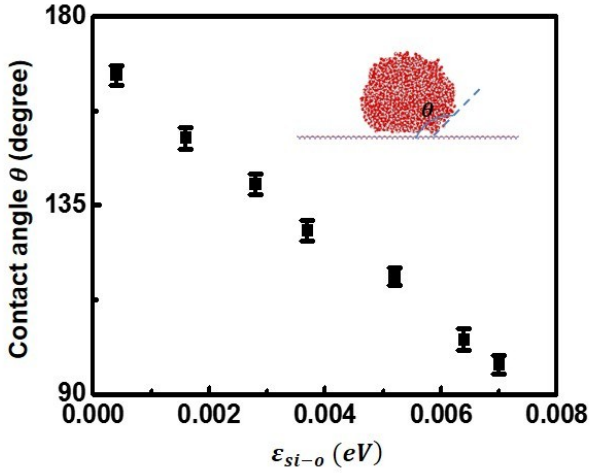

Figure S1 Variation of surface wettability represented by the contact angle θ with Si-O interactive well depth ε_{Si-O}. The inset illustrates the contact angle of liquid droplet on a solid surface (side view).

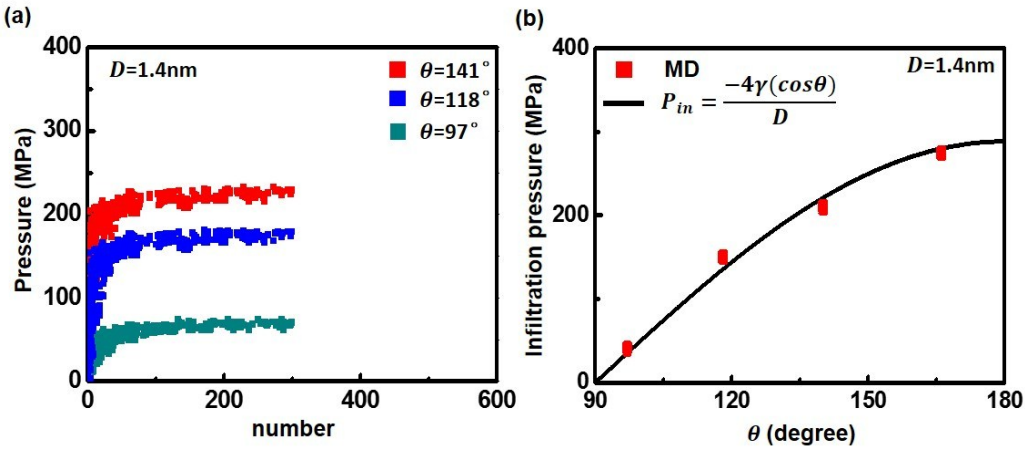

Figure S2 (a) Variation of the number of infiltrated water molecules into a SNT as a function of applied pressure for different surface wettability. **(b)** Critical liquid infiltration pressure versus contact angle θ. The diameter of SNT: $D = 1.4nm$.

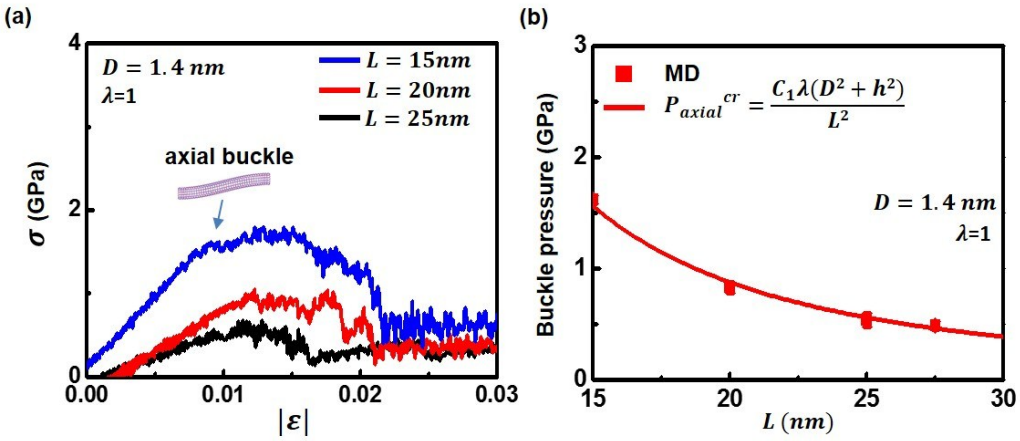

Figure S3 **(a)** Stress-strain curves of SNT under uniaxial compression for different tube length L. **(b)** Critical axial buckling pressure of SNT under uniaxial compression versus tube length L. Tube diameter $D = 1.4nm$ and the deformation energy factor $\lambda = 1$

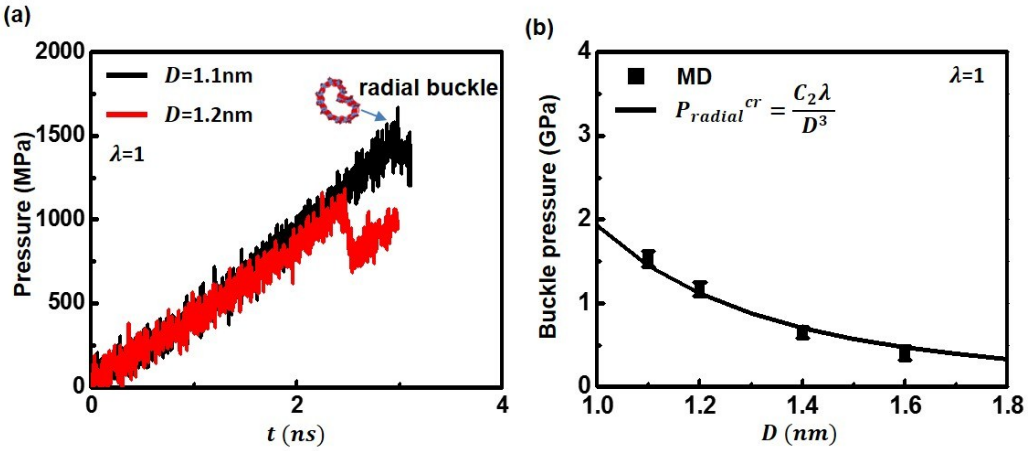

Figure S4 **(a)** Pressure versus simulation time of SNT under hydrostatic compression for different tube diameter D. **(b)** Critical radial buckling pressure of SNT under hydrostatic compression versus tube diameter D. Tube length $L = 15\ nm$ and the deformation energy factor $\lambda = 1$

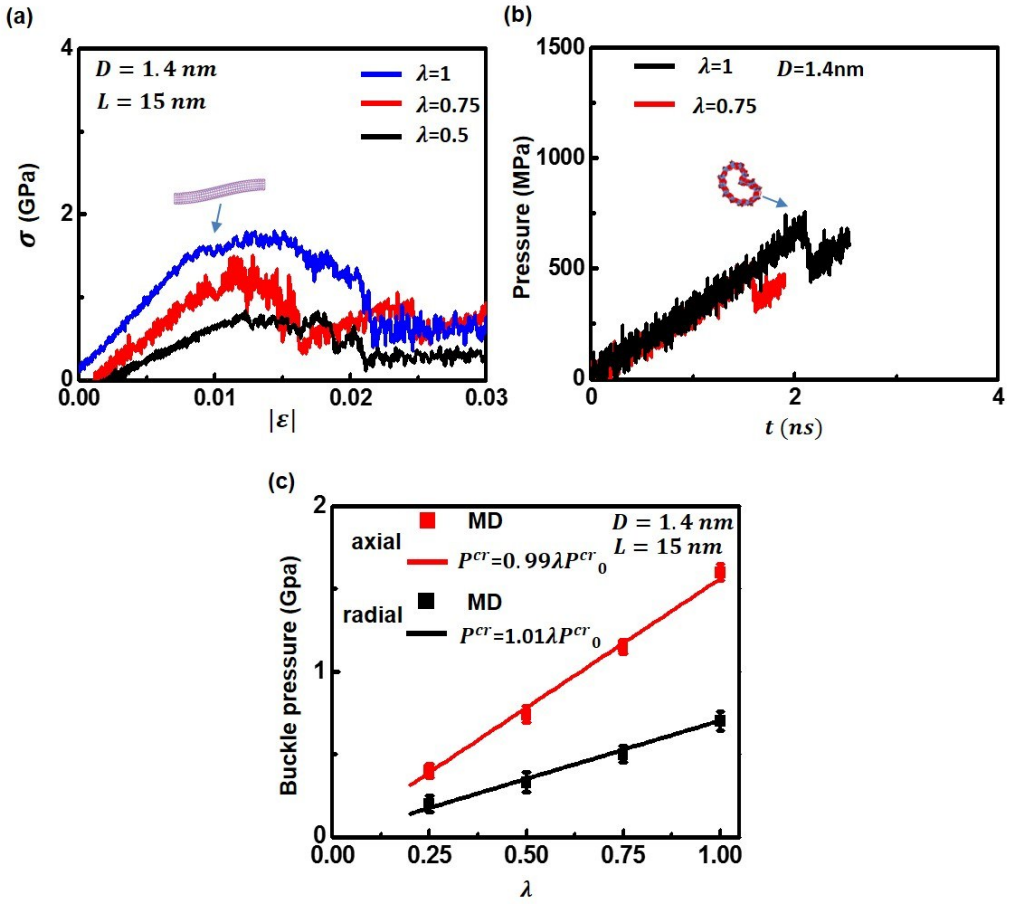

Figure S5 (**a**) Stress-strain curves of SNT under uniaxial compression for different deformation energy. **(b)** Pressure versus simulation time of SNT under hydrostatic compression for different deformation energy. **(c)** Variation of critical buckling pressure of SNT as a function of deformation energy tuning factor λ. Tube diameter $D = 1.4nm$ and length $L = 15nm$.

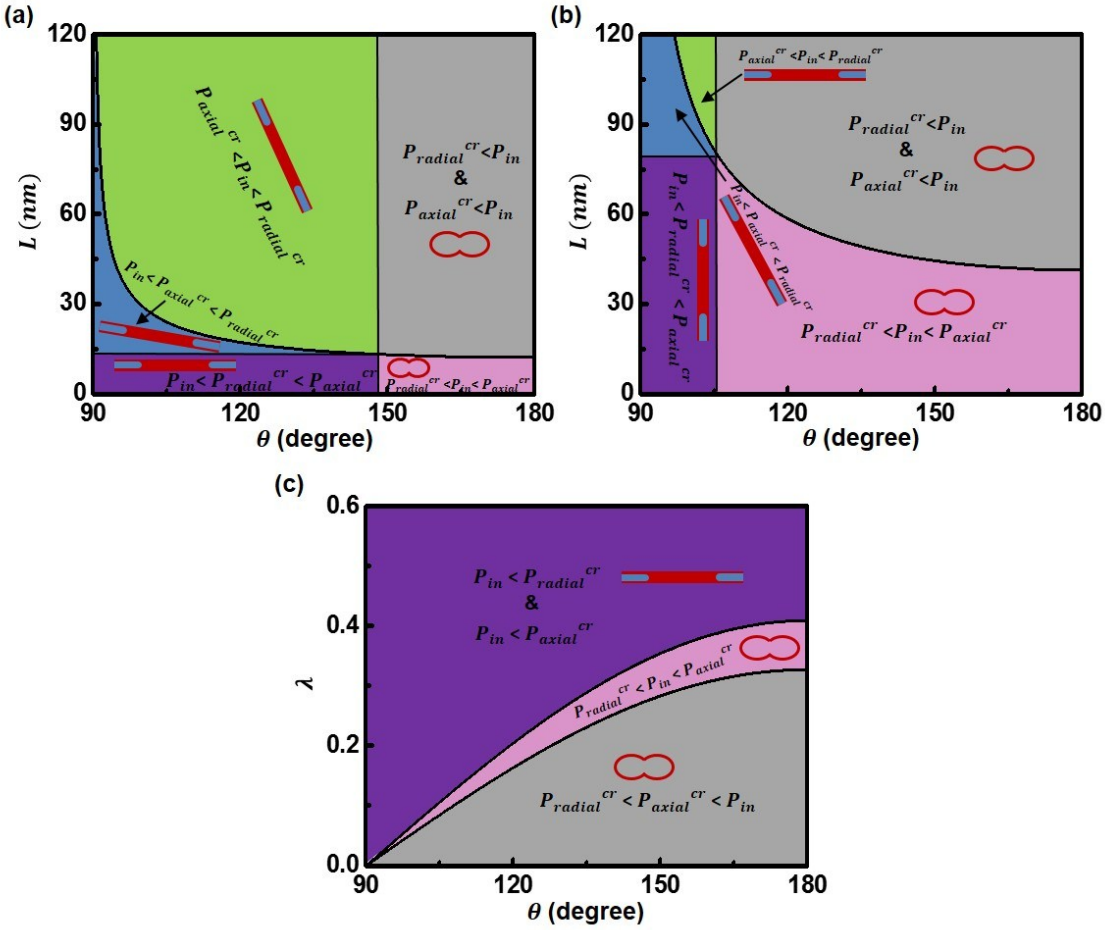

Figure S6 (**a**) Quantitative relation among critical pressure for liquid infiltration P_{in}, axial buckle P_{axial}^{cr} and radial collapse P_{radial}^{cr}, with variation of surface wettability represented by contact angle θ and tube length L. The tube diameter $D = 1\ nm$ and the deformation energy factor $\lambda = 0.3$. **(b)** Quantitative relation among P_{in}, P_{axial}^{cr} and P_{radial}^{cr}, with variation of contact angle θ and tube length L. The tube diameter $D = 2.4\ nm$ and the deformation energy factor $\lambda = 0.3$. **(c)** Quantitative relation among P_{in}, P_{axial}^{cr} and P_{radial}^{cr}, with variation of contact angle θ and deformation energy factor λ. The tube length $L = 20\ nm$ and diameter $D = 1.4\ nm$.

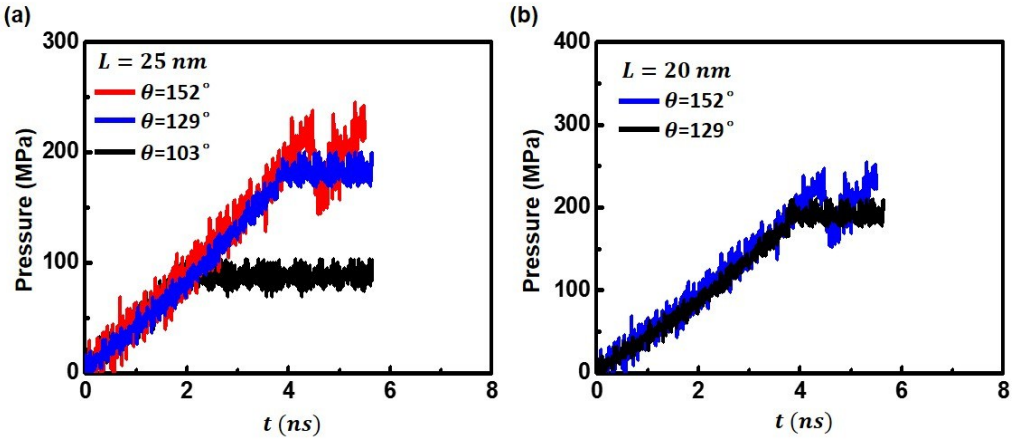

Figure S7 Water pressure versus simulation time for different surface wettability condition. With the length of nanotube **(a)** $L = 25nm$. **(b)** $L = 20nm$.

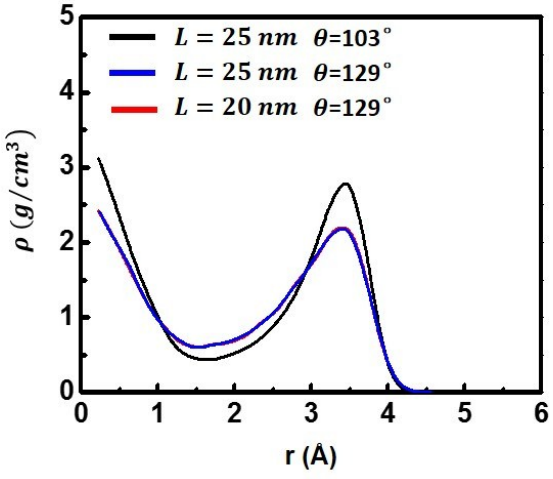

Figure S8 Radial density profiles of water confined in SNT with diameter $D = 1.4nm$. The left axis is aligned with the tube center axis.

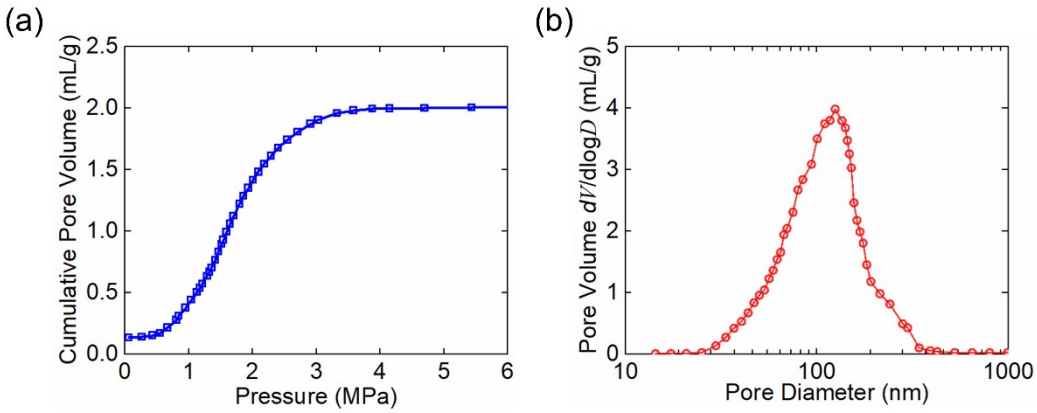

Figure S9 (a) Cumulative volume of the intruded water as a function of applied external pressure. (b) Pore size distribution of the nanoporous silica gel used in this study.

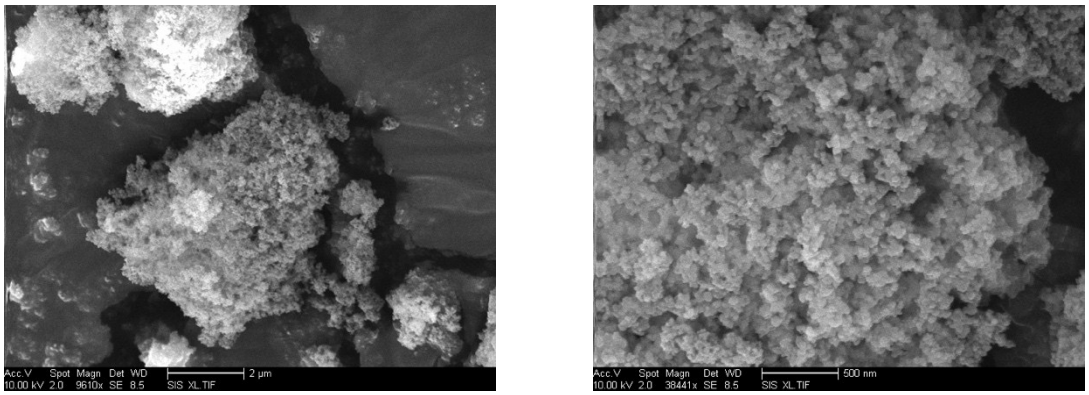

Figure S10 SEM photos of the silica gel containing 3-D nanoporous structure.